Editors' Suggestion

Error detection without postselection in adaptive quantum circuits

Eli Chertkov,* Andrew C. Potter, David Hayes, and Michael Foss-Feig
Quantinuum, 303 South Technology Court, Broomfield, Colorado 80021, USA

(Received 9 October 2025; accepted 12 March 2026; published 16 April 2026)

Current quantum computers are limited by errors, but have not yet achieved the scale required to benefit from active error correction in large computations. We show how simulations of dissipative quantum circuits can benefit from error *detection*. In particular, we use Quantinuum's H2 quantum computer to perform 24-qubit logical simulations of a nonequilibrium phase transition using many [[4,2,2]] code blocks. Importantly, by converting detected errors into random resets, which are an intended part of the dissipative quantum dynamics being studied, we avoid any postselection in our simulations, thereby eliminating the exponential cost typically associated with error detection. The encoded simulations perform near breakeven with unencoded simulations at short times.

DOI: 10.1103/6b14-7wkt

I. INTRODUCTION

Large-scale implementations of quantum error correction (QEC) in digital quantum computers are essential for realizing scalable quantum computation. However, QEC requires substantial overheads in quantum resources [1], creating a large barrier to its application in near-term resource-limited devices. Quantum error detection (QED), which involves using a logical encoding to only detect but not correct errors, has a substantially smaller overhead than QEC and provides some of the same benefits, though is generally not scalable. The standard way of using QED—postselecting on circuit realizations with no detected errors—incurs an exponential run-time overhead [2–13]. In this work, we present and experimentally demonstrate a scalable error detection protocol that has no postselection overhead when applied to the quantum simulation of certain dissipative quantum circuits (see Fig. 1).

The dissipative quantum circuit we focus on is a quantum variant of a classical model known as the contact process [14]. The classical contact process is a stochastic process, similar to a cellular automaton, that describes how a disease spreads in a population. The model has been found to exhibit a nonequilibrium phase transition, a type of phase transition that occurs far from thermal equilibrium [15–18], in the directed percolation (DP) universality class [16,19]. Recent studies have quantized the contact process to understand whether quantum fluctuations affect the critical physics, arguing that the quantum models do not follow DP universality [20–23]. Chertkov *et al.* [24] studied a dissipative quantum circuit version of the contact process, called the Floquet quantum contact process (FQCP), that contains periodic unitary evolution followed by dissipative mid-circuit random resets. Through a numerical study and an experimental demonstration on Quantinuum's H1 quantum computer, they found that the FQCP appeared to be in the DP universality class [24]. In this work, we study a slightly modified variant of the FQCP model near its critical point.

The phase transition that occurs in the dissipative circuit, also sometimes referred to as an absorbing state transition, also has connections with measurement-induced phase transitions (MIPTs) [25,26]. The MIPT is a phase transition that can be detected through the entanglement properties of quantum trajectories in circuits with mid-circuit measurements. Since the MIPT properties are trajectory dependent, studying it on a quantum computer encounters an exponential postselection overhead. Recently, numerous works have explored absorbing state transitions in quantum circuits, which have random mid-circuit resets and no postselection overhead, to understand their connections to the MIPT [27–33]. Generally, it has been found that quantum circuits exhibiting absorbing state transitions also contain MIPTs in their "active" phase [29–31]. We expect the same to be true in our model.

In this work, we implement the contact process dissipative circuit using many copies of the [[4,2,2]] code [34,35], the smallest example of an error detecting code, on Quantinuum's H2 56-qubit trapped-ion quantum computer [36,37]. Our circuit is adaptive, with hardware errors detected by [[4,2,2]] code blocks used to trigger the random resets in the circuit. We show that the protocol is scalable and use the adaptive logical circuits to measure quantitatively accurate observables near the phase transition that appear to break even with the results from physical circuits.

II. QUANTUM ERROR DETECTION CODE

In this work, we use an $[[n, k, d]] = [[4, 2, 2]]$ code—a quantum error detection code that encodes $k = 2$ logical qubits into $n = 4$ physical qubits. Since it is a distance $d = 2$ code, it can detect (but not correct) a single error. It is the smallest code capable of protecting quantum information and

*Contact author: eli.chertkov@quantinuum.com

Published by the American Physical Society under the terms of the Creative Commons Attribution 4.0 International license. Further distribution of this work must maintain attribution to the author(s) and the published article's title, journal citation, and DOI.

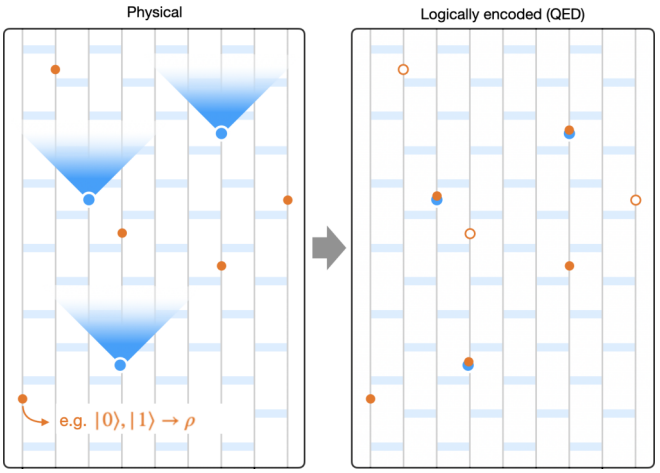


FIG. 1. How error detection can be used to remove errors without postselection in a quantum circuit with random resets (e.g., to a mixed state ρ). (Left) In the physical circuit, resets (orange) are randomly inserted and hardware errors (blue) occur randomly, spreading and corrupting the circuit's output. (Right) In the logical circuit encoded into an error detection code, hardware errors can be detected and converted into resets, preventing the spread of errors without needing to discard the circuit realization. Note that the probability of a reset is now increased by the detection events, so the injected reset rate needs to be decreased to compensate.

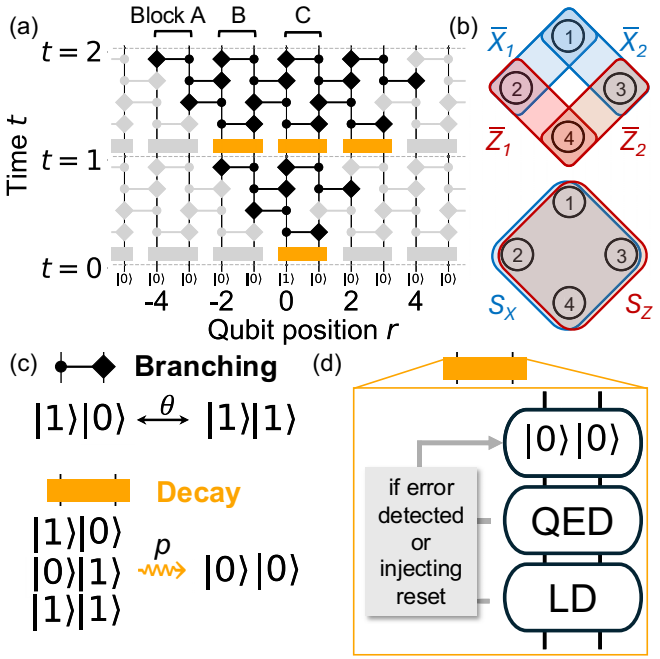


FIG. 2. (a) The dissipative quantum circuit studied in this work, encoded into multiple [[4,2,2]] quantum error detection code blocks. Each qubit shown is a logical qubit and gates are logical gates (the encoding using physical qubits is not shown here). The two-qubit gates are controlled-$R_x(\theta)$ rotation gates. The orange boxes are random two-qubit resets that occur with probability p. (b) The [[4,2,2]] code's logical Pauli operators $\bar{Z}_{1/2}, \bar{X}_{1/2}$ and stabilizers $S_{Z/X}$. Gray color indicates quantum operations that act as identity on the input state and are not applied. (c) The two competing processes in the circuit acting on computational basis states, a branching process that spreads $|1\rangle$ states to other qubits (controlled by θ) and a decay process that causes $|1\rangle$ states to decay to $|0\rangle$ states (at a rate controlled by p). (d) Using an error detection code, the circuit can be made adaptive so that random resets are intentionally injected at random or are triggered by a leakage detection (LD) or an error detection (QED) event generated by quantum hardware noise.

is the smallest code in the family of $[[n, n-2, 2]]$ "Iceberg" codes [9,38]. Each [[4,2,2]] code block has two weight-4 stabilizers $S_Z = Z_1Z_2Z_3Z_4$, $S_X = X_1X_2X_3X_4$ and four logical operators $\bar{X}_{1,2}, \bar{Z}_{1,2}$ implemented by physical weight-2 operators, as shown in Fig. 2(b). Because logical operators are weight-2 (since $d = 2$), logical rotations can be implemented (non-fault-tolerantly) using a single $U_{ZZ}(\theta) = e^{-i\theta Z\otimes Z/2}$ gate, which can be implemented natively on Quantinuum hardware [24,36,37].

In the context of quantum error detection, stabilizers are typically measured one or more times during each shot and measurement results from shots with detected errors are discarded. However, in this work, we do not discard shots and therefore need to consider the logical effects of individual errors. We refer to a Pauli P that triggers (does not trigger) a stabilizer violation as a detectable (undetectable) error; similarly, a Pauli that would flip a logical measurement result is called a logical error (e.g., X_1X_2 is an undetectable logical error and X_1 is a detectable logical error if measuring $\bar{Z}_1 = Z_1Z_3$).

Operations in quantum error correction and error detection codes can be implemented in many ways, some fault-tolerant (FT) and others not [39]. In the context of the [[4,2,2]] code, an FT operation is one in which any single circuit fault causes a detectable error, i.e., which has a logical fidelity *after postselection* that scales as $\sim Bp^2$ when physical errors happen with probability $\sim Ap$ for small p. For an FT operation, there is a pseudothreshold $p_c = A/B$, which indicates the value of p below which the logical operation outperforms the physical one. In the [[4,2,2]] code, intrablock $\overline{\text{CNOT}}$, $\bar{H} \otimes \bar{H}$ gates as well as interblock pairs of transversal CNOT gates are FT [3,6].

Unfortunately, implementing a universal FT gate set necessarily requires significant overhead, particularly for performing small-angle rotation gates required for quantum simulation [40]. However, QEC codes can still suppress errors for operations that are non-FT. If a logical operation is not FT and fails with probability $\sim Cp$, that operation can in principle still outperform the physical one if $C < A$. This inequality is not typically satisfied for high-distance QEC codes whose logical operations have many more physical gates than their unencoded physical versions. In contrast, in the [[4,2,2]] code, the logical two-qubit (2Q) rotation $e^{-i\theta\bar{Z}_1\bar{Z}_2/2} = e^{-i\theta Z_2Z_3/2}$ can be realized as a single native $U_{ZZ}(\theta)$ whose error model contains very low probability of generating undetectable logical errors ($X \otimes X$, $Y \otimes Y$, $Z \otimes Z$ errors; see Sec. I D of the Supplemental Material [41,42]). This means that this gate, even though it is non-FT, effectively has $C \ll A$ making the non-FT gate (potentially) better than the physical gate. However, non-FT gates can spread errors pathologically, potentially converting detectable logical errors on one code block into undetectable logical errors on others (see Sec. I C of the Supplemental Material [42] for an example).

For the remainder of the paper, we drop the overline notation for logical operators and states. Operators and states are at the logical level unless stated otherwise.

III. QUANTUM CONTACT PROCESS MODEL

Using the [[4,2,2]] code, we encode the dynamics of a one-dimensional dissipative quantum circuit analogous to the classical contact process [14] that undergoes an absorbing state phase transition [16,18]. The contact process circuit [see Fig. 2(a)] is a time-periodic quantum channel $\mathcal{E}(\rho) = (\mathcal{U}_\theta \mathcal{R}_p)^t$ made of unitaries $\mathcal{U}_\theta(\rho) = U_\theta \rho U_\theta^\dagger$ defined by an angle θ and random reset quantum channels $\mathcal{R}_p$ defined by the probability p, similar to the model introduced in Ref. [24]. The unitary operator U_θ contains four alternating layers of controlled-rotation gates $CR_x(\theta) = e^{-\frac{i}{4}\theta(1-Z)\otimes X}$, and the random reset channel $\mathcal{R}_p = \prod_{k=1}^{L/2} \mathcal{R}_{2k,2k+1}$ consists of a single layer of *two-qubit* random reset channels $\mathcal{R}_{j,j+1}(\rho^{(2)}) = (1-p)\rho^{(2)}_{j,j+1} + p|00\rangle\langle 00|_{j,j+1}$. Importantly, both $\mathcal{U}_\theta$ and $\mathcal{R}_p$ preserve the $|0\cdots 0\rangle$ product state, which is called the absorbing state.

The competition between the unitary evolution, which causes spreading of $|1\rangle$ (active) states among qubits, and the dissipation, which causes decay to the $|0\rangle$ (inactive) state [see Fig. 2(c)], results in an absorbing state transition at a critical p_c in the directed percolation universality class. In our experiments, we examine the propagation of a single active state in the center of the chain [see Fig. 2(a)]. For $p < p_c$, the model is in the "active" phase and active sites proliferate over time. For $p > p_c$, the model is in the "absorbing" phase and active sites decay away so that the system falls into the absorbing state, which it cannot escape from. At the $p = p_c$ critical point, active sites still proliferate, though in a self-similar fractal way with power-law scaling governed by DP critical exponents [16,18,19]. In studies of similar continuous-time models, it was argued [20–22] that quantum effects modified the critical exponents from the DP values. In classical numerical simulations for this model (see Sec. II of the Supplemental Material [42]) and its previous version [24], we find the exponents are consistent with DP.

In this work, we use a contact process model with two-qubit resets in order to match the two-qubit code block of the [[4,2,2]] code. Since the number of qubits involved in the reset does not alter any of the universal features of the model such as spatial locality, dimensionality, or structure of the absorbing state, we expect the phase transition in this model to fall into the same universality class as that of its single-qubit-reset version. As described in Sec. I B of the Supplemental Material [42], logical resets, error detection, and measurements are implemented fault-tolerantly. However, to avoid the prohibitive resource overhead of FT magic state injection [1], we implement the non-Clifford two-qubit gates (both within a code block and between code blocks) in a non-FT way, which ultimately limits the accuracy of our final results. The state preparation, error detection, and measurement require ancilla qubits. We use only four ancilla qubits, which we reset and reuse for each of the relevant logical operations, in order to reduce the effects of memory errors. The H2 device implements two-qubit gates in batches of four and using more ancilla can lead to additional transport time and therefore additional accrual of memory errors on idling qubits.

We use qubit reuse compilation [43–49] at the logical level, which allows us to reduce the qubit resources required to execute the circuit by opportunistically resetting and reusing logical code blocks (see Sec. III A of the Supplemental Material [42]). Without qubit reuse, the largest logical circuits that we run would require 52 physical qubits (including four ancilla). Instead, with qubit reuse, we ran them on the H2 quantum computer using only 28 physical qubits [see Fig. 3(b)].

IV. QUANTUM CIRCUITS THAT ADAPT TO NOISE

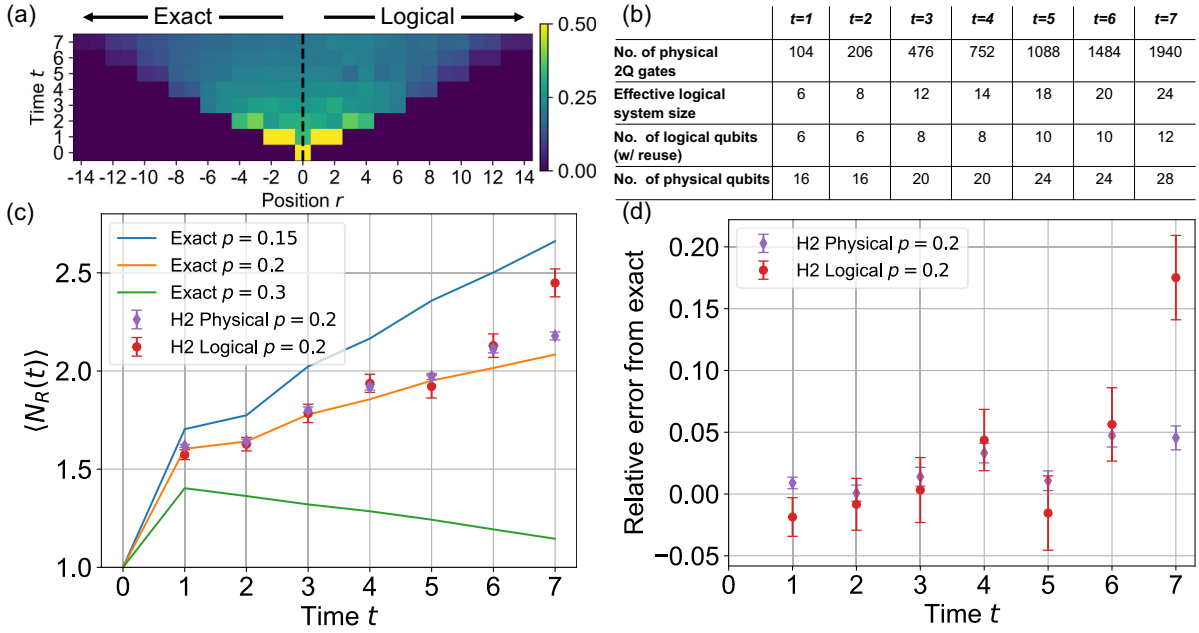
We avoid the exponential postselection penalty of quantum error detection by using an adaptive quantum circuit whose dynamics are controlled by the mid-circuit error detection measurements. As shown in Fig. 2(a), in each time step of the contact process circuit (every four layers of gates) a layer of random two-qubit resets occurs that resets each code block with probability p. In our logical circuit, we perform stabilizer measurements and leakage detection measurements [37,50,51] of each code block right before the random resets are applied. As shown in Fig. 2(d), if a stabilizer violation or leakage error (or detection gadget error) is detected, then that code block is reset to $|00\rangle$. The probability of an error being detected and converted to a reset $p_{\text{detect}}(r,t)$ is a function of the gate error model, circuit structure, and memory error induced by ion transport. In addition to the "detected resets" directly correlated to the error detection events, we also inject resets randomly with probability p_{inject} by generating random numbers and conditioning the random resets based on their values. We generate the random numbers using the quantum computer itself before the start of the calculation, as done in Ref. [24].

Given a target reset rate p for our quantum circuit, with this protocol $p_{\text{detect}}(r,t) \leqslant p$ must hold for all space-time points. One can in principle use this protocol when $p_{\text{detect}} > p$ by discarding enough shots to lower the detection probability, but this creates an exponential postselection overhead that the protocol was designed to avoid, so we do not consider this here. We run this adaptive protocol in two steps: a calibration run and a main run. In the calibration run, we do not inject any resets but only allow for resets generated by detection events and thereby obtain a measure for $p_{\text{detect}}(r,t)$. In the main run, we inject resets at the rate

$$p_{\text{inject}}(r,t) = \frac{p - p_{\text{detect}}(r,t)}{1 - p_{\text{detect}}(r,t)} \tag{1}$$

chosen so that probability of a reset occurring from either a detection or an injection event is p. In this protocol, we are assuming that detected resets are uncorrelated with one another and that injected resets do not appreciably affect the error detection rate, which empirically appears to hold in our results.

When a detected reset occurs in a code block, the corrupted logical state is replaced by an uncorrupted $|00\rangle$ state, thereby preventing the further impact of that error in the code block without any postselection. However, due to the non-FT in-



	t=1	t=2	t=3	t=4	t=5	t=6	t=7
No. of physical 2Q gates	104	206	476	752	1088	1484	1940
Effective logical system size	6	8	12	14	18	20	24
No. of logical qubits (w/ reuse)	6	6	8	8	10	10	12
No. of physical qubits	16	16	20	20	24	24	28

FIG. 3. (a) The active-site density profile $\langle n(r,t)\rangle$ for $r \geqslant 0$ obtained from the logical circuit run on H2 compared with the exact profile computed from classical numerics (reflected about $r = 0$). Note that $\langle n(0,0)\rangle = 1$, which is outside of the range of the colorbar. (b) The 2Q gate and qubit overheads of the logical circuits with and without qubit reuse. (c) The experimental results obtained on H2. The total number of active sites on the right half of the system vs time, comparing physical (purple diamonds) and logical results (red circles) against classical exact numerics (solid lines). (d) The relative error of the observable in panel (c) from the exact result for the logical and physical circuits.

terblock two-qubit gates in the model, the detectable error that caused the reset can propagate into *undetectable* logical errors on other code blocks that are left unmitigated.

V. EXPERIMENTAL RESULTS

We implement the above-described contact process circuits on Quantinuum's H2-2 trapped-ion quantum computer, which has high-fidelity mid-circuit measurements, resets, and classical feedforward capabilities—crucial features for executing these adaptive circuits.

We time evolve an initial product state $|\psi(0)\rangle = |0\cdots010\cdots0\rangle$, with a single active site at position $r = 0$ for times $t = 1, 2, \ldots, 7$ under the contact process dynamics with parameters $\theta = 3\pi/4$ (same as Ref. [24], far from the Clifford point at $\theta = \pi/2$) and $p = 0.2$. This parameter is near the critical point of the model determined from classical numerics (see Sec. II B of the Supplemental Material [42]). We perform two sets of experiments, one with the adaptive logical circuit encoded into many [[4,2,2]] code blocks and one with the physical unencoded circuit. The physical circuit only has injected resets and also uses qubit reuse. For each time t, we measure the spatial profile of the active-site density $n(r) = |1\rangle\langle 1|_r = (I - Z_r)/2$ and the total number of active sites on the right half of the system $N_R = \sum_{r\geqslant 0} n(r)$, which contain information about the critical spreading of active sites. For the logical circuits, we run 1000 shots at each time step for both the calibration run and main runs; for the physical circuits, we run 10 000 shots at each time step. The qubit number and physical two-qubit gate counts of the logical circuit are listed in Fig. 3(b) [42]. We only perform experiments at a single p value due to limited availability of the H2 hardware.

Figure 3(a) shows a heatmap of the active-site density profile obtained from the logical circuits (right) compared with exact classical density matrix simulations (left). Visually, we see that the agreement is quite good with the logical circuit clearly displaying quantitatively accurate subballistic spreading of active sites. Figure 3(c) shows the number of active sites versus time measured for the logical and physical circuits run on H2 compared with exact numerics. All error bars reported are standard errors obtained from bootstrap resampling using 200 resamples. Below the transition (blue) $\langle N_R(t)\rangle$ should grow linearly, above the transition (green) $\langle N_R(t)\rangle$ should decay to zero, and near the transition (orange) $\langle N_R(t)\rangle \sim t^{\Theta}$ with DP exponent [19] $\Theta = 0.313\,686(8)$. Figure 3(d) shows the relative error in this observable between logical and physical from exact. We see that for times $t = 1, 2, 3, 5$ the logical and physical circuits agree within error bars with each other and with the numerically exact curve. For $t = 4, 6$, both physical and logical results agree within error bars with each other, but differ by $\gtrsim$2 standard errors from the exact result. Finally, at $t = 7$, the logical result differs significantly more from exact than the physical result. We attribute this strong deviation at $t = 7$ to accumulation of memory/idling errors: Since H2-2 can execute two-qubit gates in batches of at most four, and the number of gates per circuit layer grows linearly with simulation time t [see Fig. 2(a)], the delay time and memory error per circuit layer correspondingly grows as $\sim t$. This ultimately sets a practical limit on the maximal achievable simulation time depth t. Note that while the physical circuits also have memory errors that scale as $\sim t$, the prefactor is much larger in the logical circuit because logical operations require many more physical gates and thereby many more ion transport operations. Ultimately, we see that our results are consistent

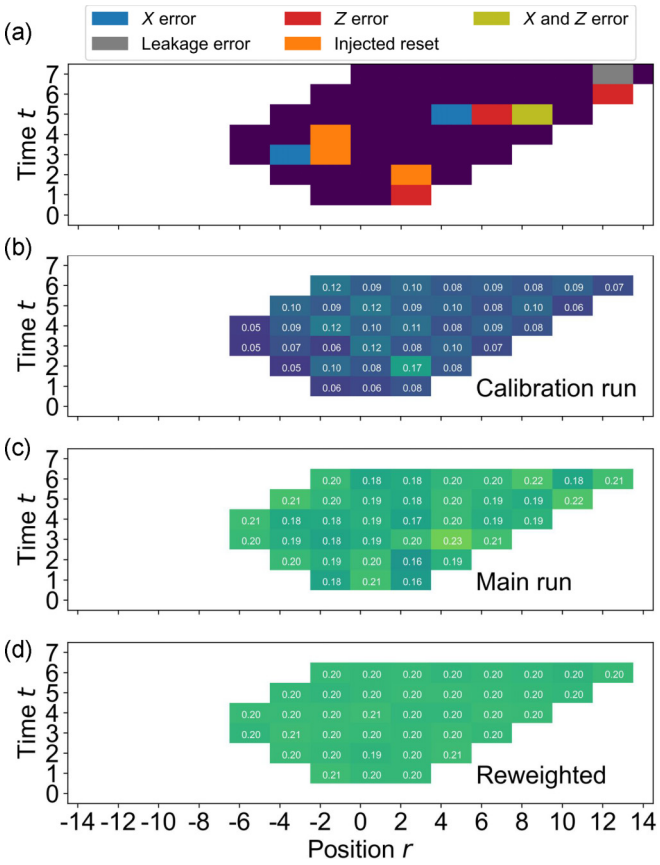


FIG. 4. (a) The space-time record of error detection events and injected resets for one shot of a $t = 7$, $p = 0.2$ circuit run on H2. (b) The average space-time probabilities of detecting an error in the calibration run. (c) The average space-time probabilities of resetting a code block in the main run, which includes injected resets as well as detected resets. (d) The average space-time probabilities of resetting a code block after using the reweighting scheme.

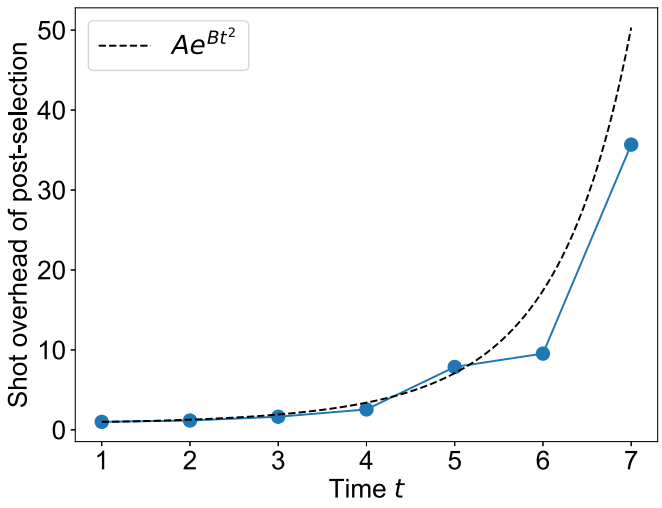


FIG. 5. The shot overhead required to perform postselection instead of the post-selection-free protocol on our experiments. The function Ae^{Bt^2} is shown as a guide to the eye to indicate the scaling with time t.

with the logical circuit breaking even with the physical circuit for $t \leqslant 6$.

In addition to the observables, we also inspect the reset rates obtained in the adaptive logical circuits to verify that resets are properly sampled. Figure 4(a) shows an example record of error detection outcomes obtained in one shot on the H2 quantum computer. In this record, we can see the space-time locations of both detected and injected resets. For the calibration run at time $t = 7$, if we average over all shots we obtain the results in Fig. 4(b), which shows the average error detection rate (for all types of errors) at all space-time points. The resulting reset rates are visibly inhomogeneous in space and time, predominately due to memory error accumulated during ion transport in the qubit reuse compilation. In the Supplemental Material [42], we discuss the various error mitigation strategies we applied to reduce the memory error, including dynamical decoupling [52], logical basis rotation, and Clifford deformation [53]. With the error mitigation, we were able to keep $p_{\text{detect}}(r,t)$ below the target $p = 0.2$ value, allowing us to access the critical point of the model in error detected circuits without postselection. Figure 4(c) shows the main-run reset probabilities at each space-time point, with typical error bars on individual space-time points around 0.01 from finite sampling. During this run, resets were injected according to Eq. (1) using the $p_{\text{detect}}(r,t)$ obtained in the calibration run shown in Fig. 4(b). The resulting reset probabilities are more homogeneous and closer to $p = 0.2$; however, certain points significantly deviate from this target value, which we attribute to imperfections in the calibration due to either statistical errors from finite sampling or drift in the underlying error model between the calibration and main runs (which were always run back-to-back in time). In an attempt to fix the residual discrepancies between the sampled reset rates and the target one, we implemented an importance-sampling-based reweighting scheme, described in Sec. III C of the Supplemental Material [42], that ascribes a weight to each shot based on the ratio of its empirical probability compared to the ideal probability and computes observable values using a weighted average. Upon reweighting, the reset probabilities become homogenous and close to the target value of $p = 0.2$ [see Fig. 4(d)]. The logical observables in Fig. 3 use the reweighting method.

From the error detection records obtained during our experiments, we estimate the savings of our post-selection-free protocol over standard postselection. For each experiment at time t, our measurement of the error detection probability at each space-time point $p_{\text{detect}}(r,t)$ [see Fig. 4(b)] can be used to estimate the postselection acceptance probability of detecting no error in each shot $p_{\text{accept}} = \prod_{(r,t)}(1 - p_{\text{detect}}(r,t))$. The shot overhead of postselection over our protocol, i.e., the additional factor of shots needed to obtain the same error bars, is then $1/p_{\text{accept}}$. Since the number of space-time points grows as $\sim t^2$ and assuming that $p_{\text{detect}}(r,t)$ is uniform in space, we would expect the shot overhead to grow exponentially as $\sim(1 - p_{\text{detect}})^{-t^2}$. Our experimental estimate of the shot overhead, shown in Fig. 5, is consistent with this scaling and demonstrates the enormous savings of avoiding postselection.

VI. DISCUSSION

We demonstrate a scalable use of quantum error detecting codes to adaptively implement a logical simulation of a dissipative quantum circuit that avoids postselection. Essentially, hardware errors are used as a source of randomness to implement random resets that exist in the dissipative circuit model of interest. This demonstration relied heavily on the high-fidelity, low-crosstalk, and fast mid-circuit measurements and resets in the Quantinuum trapped-ion hardware, as well as the classical feedforward functionality.

We show that the logical circuits we execute on the H2 device run exponentially faster than they would with standard postselection. Moreover, they appear to break even for short times, but fail to break even at the latest time point. We believe that this is the result of two factors: (1) memory errors increasing with circuit depth due to the limited number of parallel gate operations that can be performed in the device and (2) detectable logical errors becoming undetectable logical errors in other code blocks when passing through a non-fault-tolerant interblock gate. Neither of these are fundamental issues, and they can be addressed to improve the scalability of the protocol. Concerning (1), future generations of Quantinuum hardware will have more gate zones allowing parallel two-qubit gate operations, as this is a crucial consideration for scaling up quantum error correcting codes. With more gate zones, one can also be more sparing with qubit reuse to avoid the linear-in-time scaling of memory error. Concerning (2), using a purely fault-tolerant implementation of each gate, e.g., using magic state injection, will prevent the problematic spreading of undetectable errors, though likely at a large space and time overhead. We leave these improvements, as well as improvements to other details such as our reset injection calibration procedure, for future studies.

Finally, we note that the scalable post-selection-free protocol in this work can be applied to quantum systems other than the contact process or systems with random resets [29,54–58]. In particular, it can be utilized in circuits containing quantum channels of the form $\mathcal{E}(\rho) = (1-p)\rho + p\rho'$, where ρ' is a density matrix independent of ρ. For example, $\rho' = |00\rangle\langle 00|$ corresponds to the two-qubit random reset in the contact process model and $\rho' \propto I$ corresponds to a depolarizing channel. It will be interesting future work to find examples of other post-selection-free error detection protocols that can extend to even larger classes of circuits.

ACKNOWLEDGMENTS

We acknowledge the Entire Quantinuum Team for their many contributions toward successful operation of the H2 quantum computer, and Honeywell for fabricating the trap used in this experiment. We thank Chris Self, David Amaro, Aaron Hankin, Michael Mills, Steven Moses, Natalie Brown, Ciaran Ryan-Anderson, Shival Dasu, Matthew DeCross, Reza Haghshenas, Yi-Hsiang Chen, Karl Mayer, and David Stephen for useful discussions.

DATA AVAILABILITY

The data that support the findings of this article are not publicly available. The data are available from the authors upon reasonable request.

[1] S. Bravyi and A. Kitaev, Universal quantum computation with ideal Clifford gates and noisy ancillas, Phys. Rev. A **71**, 022316 (2005).

[2] A. D. Córcoles, E. Magesan, S. J. Srinivasan, A. W. Cross, M. Steffen, J. M. Gambetta, and J. M. Chow, Demonstration of a quantum error detection code using a square lattice of four superconducting qubits, Nat. Commun. **6**, 6979 (2015).

[3] D. Gottesman, Quantum fault tolerance in small experiments, arXiv:1610.03507.

[4] C. Vuillot, Is error detection helpful on IBM 5Q chips? Quantum Inf. Comput. **18**, 0949 (2017).

[5] N. M. Linke, M. Gutierrez, K. A. Landsman, C. Figgatt, S. Debnath, K. R. Brown, and C. Monroe, Fault-tolerant quantum error detection, Sci. Adv. **3**, e1701074 (2017).

[6] R. Harper and S. T. Flammia, Fault-tolerant logical gates in the IBM quantum experience, Phys. Rev. Lett. **122**, 080504 (2019).

[7] Y. Wang *et al.*, Fault-tolerant one-bit addition with the smallest interesting color code, Sci. Adv. **10**, eado9024 (2024).

[8] D. Bluvstein *et al.*, Logical quantum processor based on reconfigurable atom arrays, Nature (London) **626**, 58 (2024).

[9] C. N. Self, M. Benedetti, and D. Amaro, Protecting expressive circuits with a quantum error detection code, Nat. Phys. **20**, 219 (2024).

[10] K. Yamamoto, S. Duffield, Y. Kikuchi, and D. M. Ramo, Demonstrating Bayesian quantum phase estimation with quantum error detection, Phys. Rev. Res. **6**, 013221 (2024).

[11] Z. He, D. Amaro, R. Shaydulin, and M. Pistoia, Performance of quantum approximate optimization with quantum error detection, Commun. Phys. **8**, 217 (2025).

[12] Y. Jin, Z. He, T. Hao, D. Amaro, S. Tannu, R. Shaydulin, and M. Pistoia, Iceberg beyond the tip: Co-compilation of a quantum error detection code and a quantum algorithm, arXiv:2504.21172.

[13] S. Dasu, S. Burton, K. Mayer, D. Amaro, J. A. Gerber, K. Gilmore, D. Gresh, D. DelVento, A. C. Potter, and D. Hayes, Breaking even with magic: Demonstration of a high-fidelity logical non-Clifford gate, arXiv:2506.14688.

[14] T. E. Harris, Contact interactions on a lattice, Ann. Prob. **2**, 969 (1974).

[15] J. Marro and R. Dickman, *Nonequilibrium Phase Transitions in Lattice Models*, Collection Alea-Saclay: Monographs and Texts in Statistical Physics (Cambridge University Press, Cambridge, 1999).

[16] H. Hinrichsen, Non-equilibrium critical phenomena and phase transitions into absorbing states, Adv. Phys. **49**, 815 (2000).

[17] G. Ódor, Universality classes in nonequilibrium lattice systems, Rev. Mod. Phys. **76**, 663 (2004).

[18] H. Hinrichsen, Non-equilibrium phase transitions, Physica A **369**, 1 (2006).

[19] I. Jensen, Low-density series expansions for directed percolation: I. A new efficient algorithm with applications to the square lattice, J. Phys. A **32**, 5233 (1999).

[20] M. Marcuzzi, M. Buchhold, S. Diehl, and I. Lesanovsky, Absorbing state phase transition with competing quantum and classical fluctuations, Phys. Rev. Lett. **116**, 245701 (2016).

[21] F. Carollo, E. Gillman, H. Weimer, and I. Lesanovsky, Critical behavior of the quantum contact process in one dimension, Phys. Rev. Lett. **123**, 100604 (2019).

[22] E. Gillman, F. Carollo, and I. Lesanovsky, Numerical simulation of critical dissipative non-equilibrium quantum systems with an absorbing state, New J. Phys. **21**, 093064 (2019).

[23] M. Jo, J. Lee, K. Choi, and B. Kahng, Absorbing phase transition with a continuously varying exponent in a quantum contact process: A neural network approach, Phys. Rev. Res. **3**, 013238 (2021).

[24] E. Chertkov, Z. Cheng, A. C. Potter, S. Gopalakrishnan, T. M. Gatterman, J. A. Gerber, K. Gilmore, D. Gresh, A. Hall, A. Hankin, M. Matheny, T. Mengle, D. Hayes, B. Neyenhuis, R. Stutz, and M. Foss-Feig, Characterizing a non-equilibrium phase transition on a quantum computer, Nat. Phys. **19**, 1799 (2023).

[25] B. Skinner, J. Ruhman, and A. Nahum, Measurement-induced phase transitions in the dynamics of entanglement, Phys. Rev. X **9**, 031009 (2019).

[26] A. C. Potter and R. Vasseur, Entanglement dynamics in hybrid quantum circuits, in *Entanglement in Spin Chains*, Quantum Science and Technology, edited by A. Bayat, S. Bose, annd H. Johannesson (Springer International Publishing, Cham, Switzerland, 2022), pp. 211–249.

[27] M. Buchhold, T. Müller, and S. Diehl, Revealing measurement-induced phase transitions by pre-selection, arXiv:2208.10506.

[28] V. Ravindranath, Y. Han, Z.-C. Yang, and X. Chen, Entanglement steering in adaptive circuits with feedback, Phys. Rev. B **108**, L041103 (2023).

[29] N. O'Dea, A. Morningstar, S. Gopalakrishnan, and V. Khemani, Entanglement and absorbing-state transitions in interactive quantum dynamics, Phys. Rev. B **109**, L020304 (2024).

[30] P. Sierant and X. Turkeshi, Controlling entanglement at absorbing state phase transitions in random circuits, Phys. Rev. Lett. **130**, 120402 (2023).

[31] P. Sierant and X. Turkeshi, Entanglement and absorbing state transitions in $(d+1)$-dimensional stabilizer circuits, Acta Phys. Pol. A **144**, 474 (2023).

[32] D. Qian and J. Wang, Steering-induced phase transition in measurement-only quantum circuits, Phys. Rev. B **109**, 024301 (2024).

[33] C. LeMaire, A. A. Allocca, J. H. Pixley, T. Iadecola, and J. H. Wilson, Separate measurement- and feedback-driven entanglement transitions in the stochastic control of chaos, Phys. Rev. B **110**, 014310 (2024).

[34] L. Vaidman, L. Goldenberg, and S. Wiesner, Error prevention scheme with four particles, Phys. Rev. A **54**, R1745 (1996).

[35] M. Grassl, T. Beth, and T. Pellizzari, Codes for the quantum erasure channel, Phys. Rev. A **56**, 33 (1997).

[36] M. DeCross *et al.*, Computational power of random quantum circuits in arbitrary geometries, Phys. Rev. X **15**, 021052 (2025).

[37] S. A. Moses *et al.*, A race-track trapped-ion quantum processor, Phys. Rev. X **13**, 041052 (2023).

[38] R. Chao and B. W. Reichardt, Fault-tolerant quantum computation with few qubits, npj Quantum Inf. **4**, 42 (2018).

[39] D. Gottesman, Opportunities and challenges in fault-tolerant quantum computation, arXiv:2210.15844.

[40] B. Eastin and E. Knill, Restrictions on transversal encoded quantum gate sets, Phys. Rev. Lett. **102**, 110502 (2009).

[41] Note that the effective logical system size can be larger than expected by two qubits, due to the constrained nature of performing qubit reuse on code blocks with two logical qubits.

[42] See Supplemental Material at http://link.aps.org/supplemental/10.1103/6b14-7wkt for additional details on the quantum error detection code, numerical simulations, and experimental error mitigation, which includes Refs. [3,4,6,24,36–38,51–53,59–62].

[43] M. DeCross, E. Chertkov, M. Kohagen, and M. Foss-Feig, Qubit-reuse compilation with mid-circuit measurement and reset, Phys. Rev. X **13**, 041057 (2023).

[44] I. H. Kim, Holographic quantum simulation, arXiv:1702.02093.

[45] M. Foss-Feig, D. Hayes, J. M. Dreiling, C. Figgatt, J. P. Gaebler, S. A. Moses, J. M. Pino, and A. C. Potter, Holographic quantum algorithms for simulating correlated spin systems, Phys. Rev. Res. **3**, 033002 (2021).

[46] F. Barratt, J. Dborin, M. Bal, V. Stojevic, F. Pollmann, and A. G. Green, Parallel quantum simulation of large systems on small NISQ computers, npj Quantum Inf. **7**, 79 (2021).

[47] E. Chertkov, J. Bohnet, D. Francois, J. Gaebler, D. Gresh, A. Hankin, K. Lee, D. Hayes, B. Neyenhuis, R. Stutz, A. C. Potter, and M. Foss-Feig, Holographic dynamics simulations with a trapped-ion quantum computer, Nat. Phys. **18**, 1074 (2022).

[48] D. Niu, R. Haghshenas, Y. Zhang, M. Foss-Feig, G. K.-L. Chan, and A. C. Potter, Holographic simulation of correlated electrons on a trapped ion quantum processor, PRX Quantum **3**, 030317 (2022).

[49] Y. Zhang, S. Jahanbani, D. Niu, R. Haghshenas, and A. C. Potter, Qubit-efficient simulation of thermal states with quantum tensor networks, Phys. Rev. B **106**, 165126 (2022).

[50] R. Stricker, D. Vodola, A. Erhard, L. Postler, M. Meth, M. Ringbauer, P. Schindler, T. Monz, M. Müller, and R. Blatt, Experimental deterministic correction of qubit loss, Nature (London) **585**, 207 (2020).

[51] R. Haghshenas *et al.*, Digital quantum magnetism at the frontier of classical simulations, arXiv:2503.20870.

[52] L. Viola, E. Knill, and S. Lloyd, Dynamical decoupling of open quantum systems, Phys. Rev. Lett. **82**, 2417 (1999).

[53] A. Dua, A. Kubica, L. Jiang, S. T. Flammia, and M. J. Gullans, Clifford-deformed surface codes, PRX Quantum **5**, 010347 (2024).

[54] G. Perfetto, F. Carollo, M. Magoni, and I. Lesanovsky, Designing nonequilibrium states of quantum matter through stochastic resetting, Phys. Rev. B **104**, L180302 (2021).

[55] M. Magoni, F. Carollo, G. Perfetto, and I. Lesanovsky, Emergent quantum correlations and collective behavior in noninteracting quantum systems subject to stochastic resetting, Phys. Rev. A **106**, 052210 (2022).

[56] G. Perfetto, F. Carollo, and I. Lesanovsky, Thermodynamics of quantum-jump trajectories of open quantum systems subject to stochastic resetting, SciPost Phys. **13**, 079 (2022).

[57] S. Wald, L. H. Yao, T. Platini, C. Hooley, and F. Carollo, Stochastic resetting in discrete-time quantum dynamics: Steady

states and correlations in few-qubit systems, Quantum **9**, 1742 (2025).

[58] Y. Ilin and I. Arad, Dissipative variational quantum algorithms for Gibbs state preparation, IEEE Trans. Quantum Eng. **6**, 1 (2025).

[59] C. Chamberland and M. E. Beverland, Flag fault-tolerant error correction with arbitrary distance codes, Quantum **2**, 53 (2018).

[60] R. Chao and B. W. Reichardt, Flag fault-tolerant error correction for any stabilizer code, PRX Quantum **1**, 010302 (2020).

[61] D. A. Lidar and K. Birgitta Whaley, Decoherence-free subspaces and subsystems, in *Irreversible Quantum Dynamics* (Springer, Berlin, 2003), pp. 83–120.

[62] Edited by S. Kais, in *Quantum Information and Computation for Chemistry* (Wiley, Hoboken, New Jersey, 2014).